Journal of Materials Chemistry A

How an angstrom-thick oxide overcoat enhances durability and activity of nanoparticle-decorated cathodes in solid oxide fuel cells

Journal:	*Journal of Materials Chemistry A*
Manuscript ID	TA-ART-03-2020-002915.R1
Article Type:	Paper
Date Submitted by the Author:	15-May-2020
Complete List of Authors:	Li, Haoyu; University of California Merced Kang, Hung-Sen; University of California, Merced Grewal, Simranjit; University of California Merced Nelson, Art; LLNL, song, Shin Ae; Korea Institute of Industrial Technology, Micro Manufacturing System Technology Center Lee, Min Hwan; University of California, Merced,

ARTICLE

How an angstrom-thick oxide overcoat enhances durability and activity of nanoparticle-decorated cathodes in solid oxide fuel cells

Received 00th January 20xx,
Accepted 00th January 20xx

DOI: 10.1039/x0xx00000x

Haoyu Li,[a] Hung-Sen Kang,[a] Simranjit Grewal,[b] Art J. Nelson,[c] Shin Ae Song[d] and Min Hwan Lee*[a,b]

In this report, we demonstrate that a uniform angstrom-level oxide overcoat (either ceria or yttria with a nominal thickness of 0.7 – 1.5 Å) by atomic layer deposition is highly effective not only in enhancing the thermal stability of underlying infiltrated ceria nanoparticles but also in facilitating electrode kinetics. By employing Sr-free electrodes and Cr-free gas environment, we focus on the thermal agglomeration as the major degradation pathway and reveal the close correlation between thermal agglomeration rate of infiltrated nanoparticles and degradation rate of electrode performance in a quantitative manner. We also provide a mechanistic perspective on the beneficial effect of the overcoat in durability and performance of solid oxide fuel cell cathodes.

Introduction

A solid oxide fuel cell (SOFC) is an attractive energy conversion system in terms of conversion efficiency, power density and fuel flexibility.[1] With the awareness of its durability and cost issues being mainly originated from their high temperature operation (usually > 800 °C), intense efforts have been made to reduce the operational temperature to an intermediate range (600 – 800 °C).[2] However, a decrease in temperature causes a significant compromise in the electrochemical kinetics in particular of the oxygen reduction reaction (ORR) occurring at the cathode.[3,4]

Infiltration of catalytically active species onto a cathodic backbone structure is a widely used approach to improve the ORR activity of intermediate temperature SOFCs.[5] This is often achieved by enhancing the electrode surface area (and thus enlarging chemisorption and charge transfer sites) and/or exposing more active sites on the surface (by infiltrating materials of high oxygen exchange rate).[6] However, the tiny infiltrated nanoparticles (NPs) naturally carry a high surface energy (due to a high percentage of low-coordination sites), making the NPs susceptible to severe agglomeration during high-temperature operation.[6,7]

Atomic layer deposition (ALD) is an emerging low-temperature chemical vapor deposition variant capable of depositing well-dispersed islands or uniform films at the atomic scale even on a substrate of extreme geometric complexity.[8,9] By leveraging the capability, researchers have successfully improved SOFC durability mainly by suppressing the agglomeration of high-surface-area electrodes[10–13] and/or dopant segregation to the surface of perovskite-based cathodes.[14,15] The beneficial effects of ALD is not limited to the operational durability; an ultrathin overcoat often enhanced ORR kinetics as well. We demonstrated earlier the effectiveness of few nanometer-thick zirconia overcoat in enhancing ORR activity and thermal stability of porous Pt cathodes[10,11] and revealed the ORR enhancement is mainly caused by a facilitation of atomic oxygen-mediated non-electrochemical processes.[11] Choi et al. reported a power enhancement by 180% via an ALD-based conformal coating of (La,Sr)$CoO_{3-\delta}$ (LSC) on a porous $La_{0.6}Sr_{0.4}Co_{0.2}Fe_{0.8}O_{3-\delta}$ (LSCF) cathode.[16] They asserted partially amorphous nature of the ALD LSC overcoat lowers the oxygen removal free energy and thus improves ORR activity. Wen et al. showed that a thin ALD zirconia layer (0.8 nm) reduces the concentration of surface oxygen vacancies, which lessens electrostatically driven segregation of Sr to the surface of LSC cathode.[14] Considering the capability of ALD to perform a conformal atomic-scale treatment on complex geometry, an ALD treatment can be best leveraged when applied to a structure of extreme surface area as opposed to conventional porous backbone structures. However, its application to a high-surface-area SOFC cathodes (e.g. infiltrated cathodes) and associated analysis is rarely reported.

In this report, we demonstrate how an angstrom-level ALD oxide overcoat affects the performance and durability of a ceria

---

[a] Department of Mechanical Engineering, University of California, Merced, 5200 N. Lake Rd. Merced, CA 95343, USA; E-mail: mlee49@ucmerced.edu
[b] Graduate Program in Materials and Biomaterials Science and Technology, University of California, Merced, 5200 N. Lake Rd. Merced, CA 95343, USA
[c] Lawrence Livermore National Laboratory Livermore, CA 94550, USA
[d] Micro/Nano Scale Manufacturing Group, Korea Institute of Industrial Technology, 143 Hanggaulro, Sangnok-gu, Ansan, Gyeonggi Province 15588, Republic of Korea

Electronic Supplementary Information (ESI) available: [details of any supplementary information available should be included here]. See DOI: 10.1039/x0xx00000x

NP-infiltrated $LaNi_{0.6}Fe_{0.4}O_{3-\delta}$ (LNF) cathode. Since LNF does not have A-site Sr, it does not suffer from Sr segregation, a major degradation mechanism,[17] simplifying the analysis of degradation in this study. The structural stability of LNF is sensitive to the Ni-to-Fe ratio,[18] but a Ni:Fe molar ratio of 6:4 is known to render an excellent stability in rhombohedral structure.[19] The NPs formed on LNF backbones are prone to agglomeration unless properly engineered due to their small sizes (5 – 20 nm). Based upon electrochemical and physical characterization of a series of infiltrated and/or ALD-treated samples, we discuss the impact of surface treatment on the morphology evolution, surface chemistry and electrode performance. In addition, we provide a quantitative analysis of NP agglomeration kinetics with and without ALD treatment and prove the close correlation between the NP agglomeration and electrode performance degradation.

Experimental

Cell preparation

All the cells are in the symmetric configuration, comprised of a YSZ electrolyte, a GDC interlayer, a surface-engineered LNF layer (namely, active layer; AL) and an additional LNF layer for current collecting. The cell area of 0.35 cm^2 is defined by the LNF layer patterned in circle. The GDC layer (~ 5 μm thick) is placed to prevent any unexpected reaction between YSZ and LNF layers that forms insulating secondary phases (e.g. $La_2Zr_2O_7$).[20] First, a GDC slurry was screen-printed on both sides of a 8 mol% YSZ electrolyte substrate (270 μm thick, FuelCellMaterials), dried at 80 °C for 1 h and sintered at 1150 °C for 3 h. Then, an LNF slurry was screen-printed onto both sides of the GDC layer, dried at 80 °C for 1 h and sintered at 850 °C for 3 h. The LNF and GDC slurries were prepared with the approach reported earlier.[21] Briefly, the LNF slurry was prepared by mixing house-made LNF powder, dispersant (Hypermer KD-1, Croda) and binder (ethyl cellulose) in terpinol. The GDC slurry was made of GDC nanopowder (FuelCellMaterials), ethyl cellulose, hypermer KD-1 and terpineol.

On top of the resulting LNF layer, infiltration (ceria) and/or ALD (yttria or ceria) was performed. Ceria infiltrated samples without an ALD treatment is categorized as Type I while ALD-treated samples without an infiltration is categorized as Type II. For ceria infiltration, 1 M aqueous solution of cerium(III) nitrate hexahydrate (99%, Aldrich) was prepared with deionized water. Sol impregnation was then performed on both sides of the cell onto the LNF backbone, let idle for 1 h under a house vacuum, and then dried at 450 °C for 0.5 h in a furnace. For ALD of ceria and yttria, tris(i-propylcyclopentadienyl)cerium(III) $[Ce(iPrCp)_3]$ and tris(methylcyclopentadienyl) yttrium(III) $[Y(MeCp)_3]$ were used as the precursors while distilled water and nitrogen was used as co-reactant and purging gas, respectively. The canister temperatures for Ce and Y were 145 °C and 150 °C with the chamber temperature of 250 °C. The pulsing time of 3 s was used for Ce and Y precursor, and 0.4 s for water. Before an ALD treatment is performed on a ceria-infiltrated LNF, a sintering process (850 °C for 2 h) can be added; the one without the additional sintering process is categorized as Type III-A and the one with the sintering process as Type III-B. Finally, an additional layer of LNF was screen-printed on top of the infiltrated and/or ALD-treated LNF layer to use as the current collecting layer. The resulting symmetric cell was and dried at 80 °C for 1 h and sintered at 850 °C for 3 h with the heating/cooling rate of 3 °C min^{-1}. For all the samples for X-ray photoelectron spectroscopy (XPS) analysis, the sintering process (850 °C for 3 h) was performed without the additional LNF layer.

A separate set of samples were prepared for X-ray diffraction (XRD) analysis to reveal the chemical information of the cathode only without being obscured by the presence of the GDC/YSZ electrolyte. To make LNF pallet-supported sample for this purpose, LNF powders was first ball-milled and pressed under a uniaxial press. After sintering the resultant LNF pallet at 850 °C for 3 h, either an infiltration or an ALD process was performed before another sintering at 850 °C for 3 h. Transmission electron microscopy (TEM) samples were prepared by grinding surface-treated LNF into powders, suspending them in ethanol and drop-casting the particle suspension upon a 3 mm lacey-carbon grid (Ted Pella).

Physical characterization

A field-emission scanning electron microscopy (SEM, Zeiss Gemini 500) was used at 3 kV to observe the microstructures. The structure and size of NPs were characterized by transmission electron microscopy and scanning transmission electron microscopy (STEM) which were recorded on a 200 kV FEI monochromated F20 UT Tecnai system. The STEM image was obtained with a convergence angle of 10 mrad and a detection angle of 30 mrad. Energy filtered transmission electron microscopy (EFTEM) was used to visualize elemental distributions. The energy dispersive X-ray spectroscopy (EDS) (Oxford X-max SDD 127eV at 50k cps) was performed on a Talos F200C G2 TEM system; X-FEG electron source, 0.18 lattice resolution and 0.30 nm point-to-point resolution was set to the tip. XPS was performed on a PHI Quantum 2000 system using a focused, monochromatic Al Kα X-ray (1486.6 eV) source for excitation and a spherical section analyzer (200 μm diameter X-ray beam incident to the surface normal; detector set at 45°). The phase and composition of samples were evaluated by XRD using a PANalytical X'Pert Pro system with Co Kα radiation (λ = 1.78897 Å).

Electrochemical characterization

Electrochemical properties were analyzed by electrical impedance spectroscopy (EIS) with 20 mV of ac perturbation at the open circuit condition (Bio-Logic SP-240) in a customized SOFC test station. Pt mesh was placed on both sides of the sample to collect current and a weight of 5 kg was applied to ensure a solid contact between the cell and current collector. Different oxygen partial pressures (pO_2) were realized by changing the ratio of O_2 and N_2 gas flow rates while maintaining the total flow rate at 100 sccm. Sample was heated at a rate of 3 °C/min and held at each temperature of test for > 30 min before

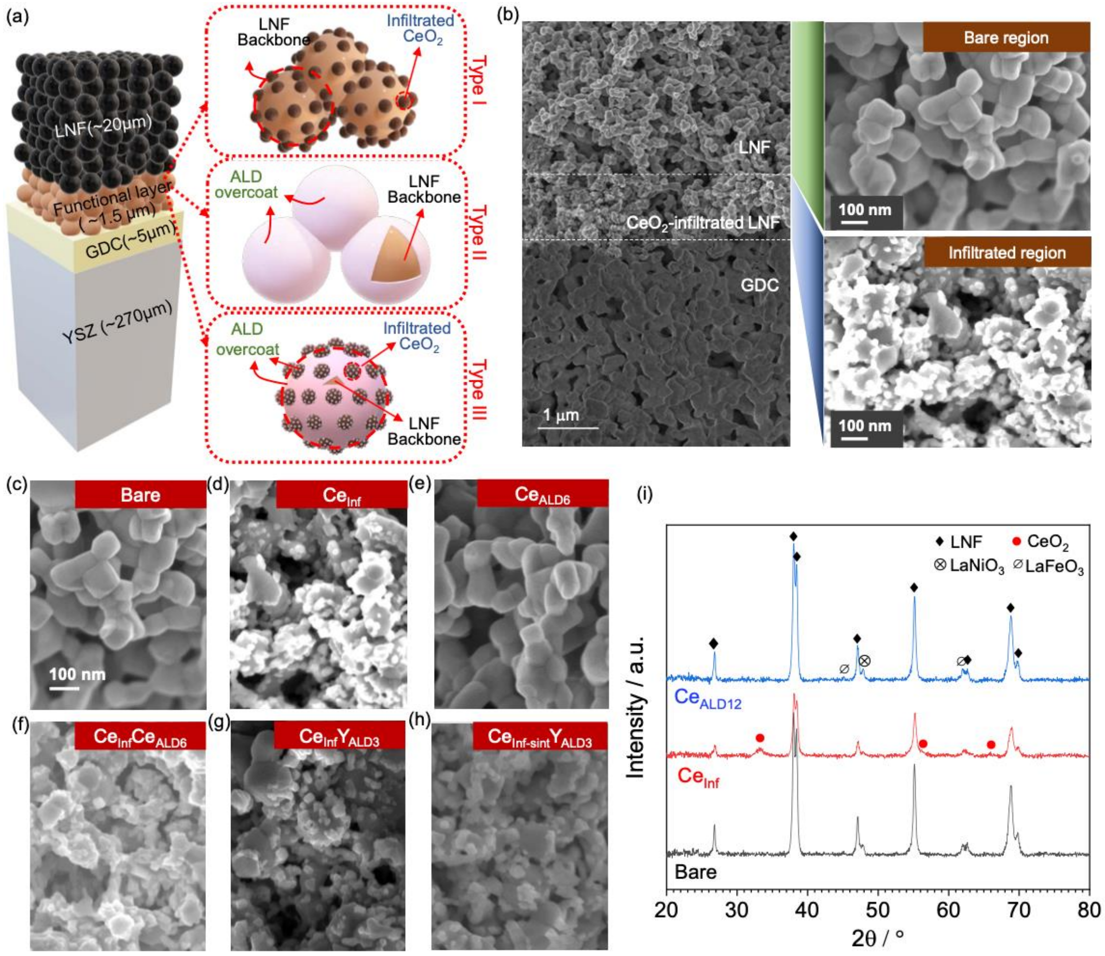

Fig. 1 (a) A schematic diagram of our cell configuration depicting three different classes of surface treatment. (b) A cross-sectional SEM image in the vicinity of LNF/GDC interface and zoomed-in images in the bare and infiltrated region of LNF backbone. (c-h) SEM images of bare, infiltrated and/or ALD-treated samples. (i) XRD spectra of bare, Ce$_{Inf}$ and Ce$_{ALD12}$ samples; obtained using Co Kα radiation (λ = 1.78897 Å).

testing. Cell durability tests were performed at 700 °C by obtaining EIS data every hour in a different customized SOFC test setup free of Cr components. O_2 gas was continuously fed into the chamber at 200 sccm throughout the test.

Results and Discussion

Three different classes of surface treatments were performed on LNF backbone as depicted in Fig. 1a: cells treated with an infiltration process only (Type I; Ce$_{Inf}$), an ALD process only (Type II; Ce$_{ALDn}$ series) and an infiltration followed by an ALD process (Type III). Within Type III, there are two sub-categories: those sintered (at 850 °C) after both an infiltration and an ALD processes are performed (namely, Type III-A; e.g. Ce$_{Inf}$Ce$_{ALDn}$), and those where an additional sintering process is inserted between the infiltration and ALD treatment (namely, Type III-B; e.g. Ce$_{Inf\text{-}sint}$Ce$_{ALDn}$). As described in the Methods section, the surface treatment (infiltration and/or ALD) was performed on a porous screen-printed LNF backbone (~10 μm). For electrochemical characterization, another ~10 μm thick LNF layer is deposited on top of the surface treated LNF layer for current collecting. The infiltrated CeO_2 NPs are mostly located in the vicinity of the GDC/LNF interface with a width of ~1.5 μm (we call it the active layer; AL), leaving the upper part of the backbone virtually uncoated as shown in Fig. 1b. This is likely due to a relatively low viscosity of precursor solution used for the infiltration, which would make the solution readily permeate through the porous LNF backbone (driven by both capillary action and gravity) and accumulate around the interface with GDC. The ceria-infiltrated cell (Type I; Ce$_{Inf}$) has 5 – 20 nm ceria NPs on the LNF backbone whose granular feature is sized ~ 100 nm (Figs. 1b and 1d). On the other hand, the ALD overcoat do not form a noticeable feature in any of the Type II (Fig. 1e) and Type III cells (Figs. 1f-h). However, after a long-term thermal exposure (260 h at 700 °C), ALD-induced ceria nanodots of 3 – 4 nm are resolved in Ce$_{Inf\text{-}sint}$Ce$_{ALDn}$ series (Type III-B) as shown in Fig. S1a-b while the feature was not observed in any other aged samples including the other Type III-B sample (Ce$_{Inf\text{-}sint}$Y$_{ALDn}$ series; Fig. S1c-d). Interestingly, the ALD ceria nanodots are preferentially formed on infiltrated ceria NPs only (in particular, more at the neck formed between infiltrated NPs)

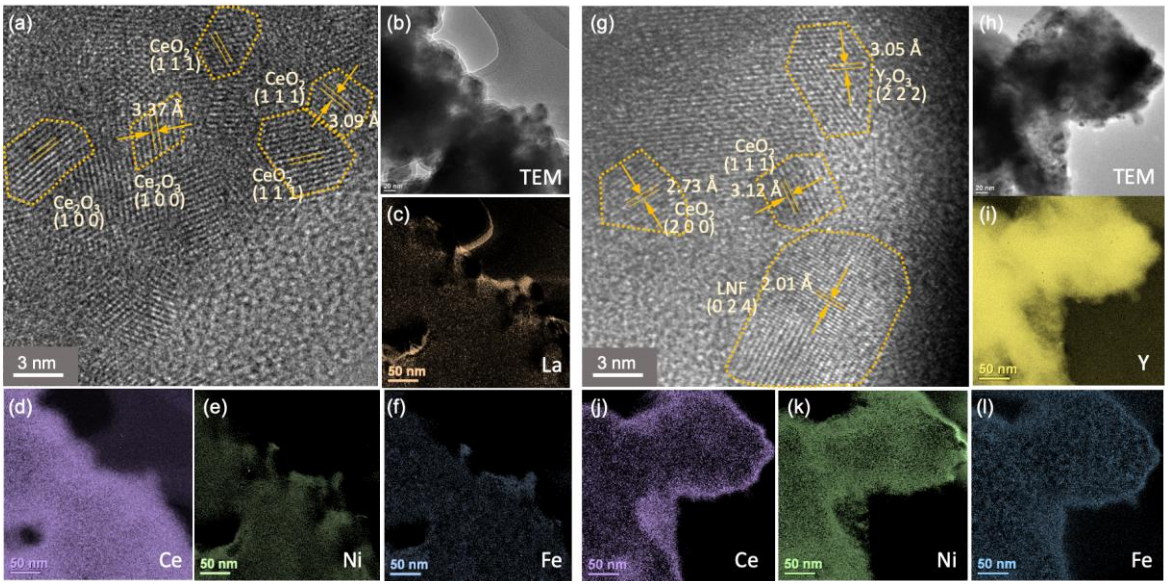

Fig. 2 HRTEM images and EFTEM elemental maps of $\mathrm{Ce_{Inf}Ce_{ALD6}}$ (a-f) and $\mathrm{Ce_{Inf}Y_{ALD3}}$ (g-l). In the HRTEM images (a, g), the boundaries of nanocrystals and identified lattice *d*-spacings are marked.

as opposed to the LNF backbone surface as shown Fig. S1a-b and schematically expressed in the "Type III" rectangle of Fig. 1a. Since the LNF backbone has a very high effective aspect ratio (~10 μm of backbone thickness versus ~ 100 nm of pore size) for the transport of ALD precursor, the ALD growth rate should be diminished with depth.[22] For this reason, the growth rate is quantified directly from the distribution of ALD-based nanodots formed in the AL (Figs. S1a-b). The growth rate estimated using this approach is 0.24 Å per cycle (see SI, "Estimation of ALD growth rate" section).

The XRD spectra (Fig. 1i) reveal that the backbone comprises mostly rhombohedral LNF (R-3c space group) with a minor presence of $\mathrm{LaNiO_3}$ and $\mathrm{LaFeO_3}$ (both R-3c space group). The $\mathrm{Ce_{Inf}}$ sample shows additional peaks corresponding to cubic $\mathrm{CeO_2}$ (Fm-3m space group) including the one at 33.3° for (1 1 1) plane. However, the ALD-coated sample ($\mathrm{Ce_{ALD12}}$) did not show a discernible ceria peak due to the tiny amount of ALD-derived ceria. This is the case for the Type-III samples; only the peaks corresponding to LNF backbone and infiltrated ceria are detected without a trace of Y from ALD in $\mathrm{Ce_{Inf}Y_{ALD15}}$ (Fig. S2).

To better resolve the surface-treated species, a set of TEM imaging and EFTEM elemental mapping was performed as shown in Fig. 2. The HRTEM images in Figs. 2a and 2g are captured at locations close to the very surface of an infiltrated ceria NP. The $\mathrm{Ce_{Inf}Ce_{ALD6}}$ (Fig. 2a) shows $\mathrm{CeO_2}$ and $\mathrm{Ce_2O_3}$ nanocrystals sized between 3 – 7 nm. Considering the XRD spectrum of $\mathrm{Ce_{Inf}}$ (Fig. 1i) showed only cubic $\mathrm{CeO_2}$ without a trace of $\mathrm{Ce_2O_3}$, the $\mathrm{Ce_2O_3}$ crystals shown in the HRTEM are likely formed in a tiny amount on the very surface by ALD. The existence of thermodynamically unstable $\mathrm{Ce_2O_3}$ is supported by a recent study by Gupta et al.[23] that showed a nucleation of $\mathrm{Ce_2O_3}$ phase in the first ~ 1.5 nm by a $\mathrm{Ce(iPrCp)_3/H_2O}$-based ceria ALD (the ALD chemistry used in this work). The Ce elemental map in Fig. 2d also indicate that ceria species are uniformly distributed throughout the surface of LNF backbone. The

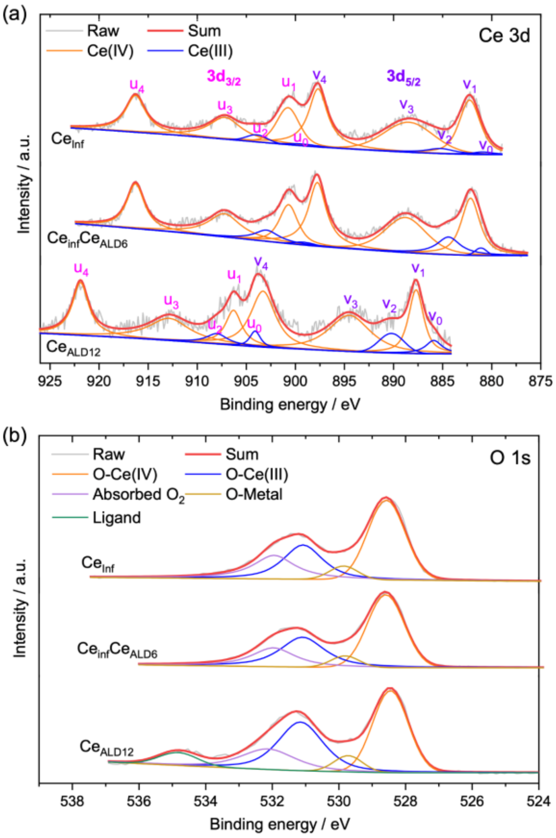

Fig. 3 Ce 3d and O 1s XPS peaks obtained from $\mathrm{Ce_{Inf}}$, $\mathrm{Ce_{ALD12}}$ and $\mathrm{Ce_{Inf}Ce_{ALD6}}$.

HRTEM of $\mathrm{Ce_{Inf}Y_{ALD3}}$ in Fig. 2g also confirms the presence of $\mathrm{Y_2O_3}$ nanocrystals formed by ALD, and the EFTEM elemental map of Y (Fig. 2i) shows its uniform distribution throughout the LNF surface; see also Figs. S3-S4 for EDS data supporting this.

XPS analysis was performed to reveal the chemical bonding states at the very surface of three samples: $\mathrm{Ce_{Inf}}$ (Type I), $\mathrm{Ce_{ALD12}}$ (Type II), and $\mathrm{Ce_{Inf}Ce_{ALD6}}$ (Type III). By applying Maslakov et al.'s approach,[24] the ratios of $\mathrm{Ce^{3+}}$ to $\mathrm{Ce^{4+}}$ are quantified to be 5.96% and 12.6% for $\mathrm{Ce_{Inf}}$ and $\mathrm{Ce_{Inf}Ce_{ALD6}}$, respectively, from the Ce 3d spectra shown in Fig. 3a (see SI "Deconvolution of XPS spectra" section and Table S1). The $\mathrm{Ce^{3+}}$ content is even higher in $\mathrm{Ce_{ALD12}}$ (13.4%). This is well aligned with the O 1s spectra in that the relative amount of O-$\mathrm{Ce^{3+}}$ in $\mathrm{Ce_{ALD12}}$ (48.3%) and $\mathrm{Ce_{Inf}Ce_{ALD6}}$ (40.2%) are larger than that of $\mathrm{Ce_{Inf}}$ (37.5%); see Table S2. A trivalent Ce can be related to either an oxygen vacancy formation in $\mathrm{CeO_{2-x}}$ or a lattice Ce in $\mathrm{Ce_2O_3}$. In either case, their unstable surfaces as compared to that of stoichiometric $\mathrm{CeO_2}$ is likely to make it advantageous in the oxygen exchange kinetics.[25] On the other hand, the Ce 3d spectrum of $\mathrm{Ce_{ALD12}}$ is shifted to a higher binding energy by an unexpectedly large margin (5.7 eV) with respect to the other two samples. Considering a new O 1s peak appearing at an unusually high binding energy (~534.8 eV; not relevant to a lattice oxygen) and a distinct difference in C 1s spectrum, but without a noticeable difference in the spectra of La 3d, Ni 2p and Fe 2p (Fig. S5), it is conjectured that the large Ce 3d binding energy shift of $\mathrm{Ce_{ALD12}}$ is originated from a strong electronegativity of unidentified ligand(s) attached to Ce.

Fig. 4 presents electrochemical data obtained from a bare sample and surface-treated samples; Nyquist plots and Arrhenius plots for all the studied samples are presented in Fig. S6. Since most samples show a single smooth arc in the Nyquist plot, a simple L-R_o-(R_p//Q_p) model (inset of Fig. 4a; see SI "EIS fitting to a single arc model" section) is used to fit all the presented impedance data; R_o, R_p, and Q_p refers to ohmic resistance, electrode polarization resistance and constant phase element (CPE), respectively; see fitted parameters in Table S3 and S4. All the resistance values are presented after a normalization by the cell area for a facile comparison. First, the bare sample (without an infiltration or ALD process) shows a large R_p (2.73 Ω $\mathrm{cm^2}$ at 700 °C) and high activation energy of electrode polarization resistance (E_a = 1.74 eV). This is mainly ascribed to the extremely small concentration of oxygen vacancies in a bare LNF (oxygen non-stoichiometry < 0.005 in the usual SOFC condition)[26] and the resulting high energy barrier for dissociative adsorption of $\mathrm{O_2}$.[21,27] A single-step infiltration ($\mathrm{Ce_{Inf}}$) decreased R_p and E_a by a significant amount (Fig. 4b). An infiltration of external hetero-species doped ceria has been reported to facilitate oxygen adsorption and dissociation kinetics.[21,28] Although we infiltrated ceria NPs without an explicit doping, we still observe a drastic improvement in oxygen electrode performance by reducing R_p from 2.73 to 0.27 Ω $\mathrm{cm^2}$ at 700 °C. This is ascribed

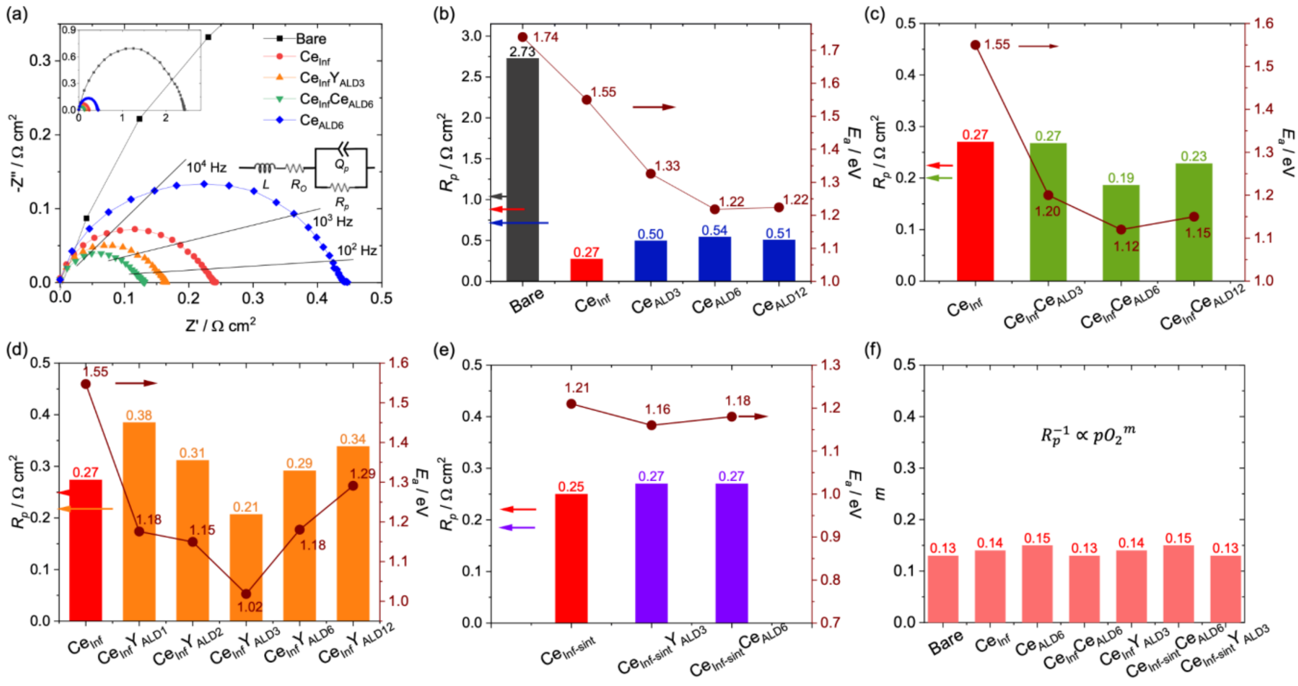

Fig. 4 (a) EIS curves of several selected samples obtained at 700 °C and the equivalent circuit used for fitting. The inset is a zoomed-out Nyquist plot to show the full spectrum of bare sample. (b-e) The fitted polarization resistances (R_p) and their activation energies (E_a); (b) Bare, $\mathrm{Ce_{Inf}}$ (Type I) and $\mathrm{Ce_{ALDn}}$ series (Type II), (c,d) $\mathrm{Ce_{Inf}Ce_{ALDn}}$ and $\mathrm{Ce_{Inf}Y_{ALDn}}$ series (Type III-A) and (e) $\mathrm{Ce_{Inf\text{-}sint}Y_{ALD3}}$ and $\mathrm{Ce_{Inf\text{-}sint}Ce_{ALD6}}$ (Type III-B). All the corresponding EIS curves and Arrhenius plots are provided in Fig. S6. (f) Reaction order (m) values obtained at 700 °C; the corresponding R_p versus $p\mathrm{O_2}$ graphs presented in Fig. S8. The inset shows the parametric meaning of m; $p\mathrm{O_2}$ is the partial pressure of $\mathrm{O_2}$ applied to the cell during measurements.

to the widely known characteristics of ceria: flexible cationic valence state and facile oxygen vacancy formation,[29] which provides reversible oxygen exchange and high oxygen storage capacity.[30,31]

A considerable decrease in R_p was achieved by a 3, 6 and 12 cycles of ceria ALD as well (Type II; Fig. 4b). With 3 cycles of ceria ALD (only 0.72 Å of nominal thickness) on a bare LNF, R_p decreased by a factor of 5.2 (down to 0.50 Ω cm^2) at 700 °C. Although the amount of performance enhancement was larger by an infiltration than by an ALD overcoat, the effect of ALD is surprising in that the volume of ceria added by a 3 cycle ALD is only ~ 0.044% of the LNF backbone (see SI, "Estimation of volumetric ratio" section); a one-step infiltration forms an oxide volume much larger than a few cycles of ALD but a small volume compared to the backbone (~ 3%).[21] No morphological corrugations by an ALD process was observed on the surface LNF backbone, either. Therefore, while it is clear that the enhancement in the electrode kinetics is enabled by a facilitation of a highly surface-specific process (as opposed to a bulk process), it cannot be ascribed to a change of surface area nor triple phase boundary area. Based upon the quantified E_a (1.22 – 1.33 eV) and reaction order values (m ~ 0.15; Fig. 4f), we ascribe the performance enhancement to a considerable facilitation of dissociation and partial reduction of O_2 (namely, "O_2 activation"), which we identified as the rate-determining step (RDS) of ORR in the backbone LNF;[21] see SI "Effect of surface treatment on the RDS" section for detailed discussion on how the surface treatment affected elemental steps and the overall activity of ORR. This is supported by the large amount of Ce^{3+} species (13.4%) in $\mathrm{Ce_{ALD12}}$, much larger than that of $\mathrm{Ce_{Inf}}$ (5.96%) as quantified by XPS. Fig. 4b shows that the R_p values of $\mathrm{Ce_{ALDn}}$ samples prepared with 3, 6 and 12 cycles of ceria ALD are similar to each other. Since the nominal thickness (the thickness estimated when assuming a perfectly uniform film) is only ~ 2.88 Å even with 12 cycles, it is likely to take a much larger number of cycles to fully passivate the LNF surface and suppress the electrode kinetics.

The impedance data of Type III-A cells are presented in Figs. 4c,d. In both $\mathrm{Ce_{Inf}Ce_{ALDn}}$ (Fig. 4c) and $\mathrm{Ce_{Inf}Y_{ALDn}}$ series (Fig. 4d), there is an optimum number of cycles for performance, presenting a V-shape behavior in the R_p versus ALD cycle relation. The $\mathrm{Ce_{Inf}Ce_{ALD6}}$ and $\mathrm{Ce_{Inf}Y_{ALD3}}$ show even lower R_p values than $\mathrm{Ce_{Inf}}$ showing the promise of further activity enhancement of infiltrated electrodes by an ALD treatment. The V-shape behavior makes good sense in that an excessive ALD overcoat will fully block the underlying catalytically active surface while a negligible amount of ALD species will make little effect on the performance. However, the reason behind the increase of R_p caused by only a single cycle ALD of yttria (Fig. 4f) is not clear at this point. It is noted that ALD treated samples show E_a values ranging 1.02 – 1.29 eV, considerably lower than that of the infiltration-only sample (1.55 eV). A synchronous behavior of E_a with R_p among the ALD-treated samples is additionally noted; the samples with minimum R_p show the smallest E_a in each sample series. These indicate a significant decrease of the barrier height for O_2 activation or even a possible shift in the RDS of oxygen reaction by an angstrom-level ALD. This is again in accordance with the XPS result showing a high Ce^{3+} content of ALD-treated samples compared to $\mathrm{Ce_{Inf}}$. On the other hand, Type III-B samples ($\mathrm{Ce_{Inf\text{-}sint}Y_{ALD3}}$ and $\mathrm{Ce_{Inf\text{-}sint}Ce_{ALD6}}$; Fig. 4e) show slightly higher R_p values than their corresponding Type III-A samples ($\mathrm{Ce_{Inf}Y_{ALD3}}$ and $\mathrm{Ce_{Inf}Ce_{ALD6}}$). This is likely because the additional sintering process performed before ALD treatment (Type III-B samples) have the infiltrated NPs agglomerated, resulting in a decrease of surface area (see Fig. 6f and the green bars in Fig. 6a-e; longer trails toward bigger NP sizes beyond ~ 40 nm is found in Type III-B samples unlike Type I and Type III-A samples).

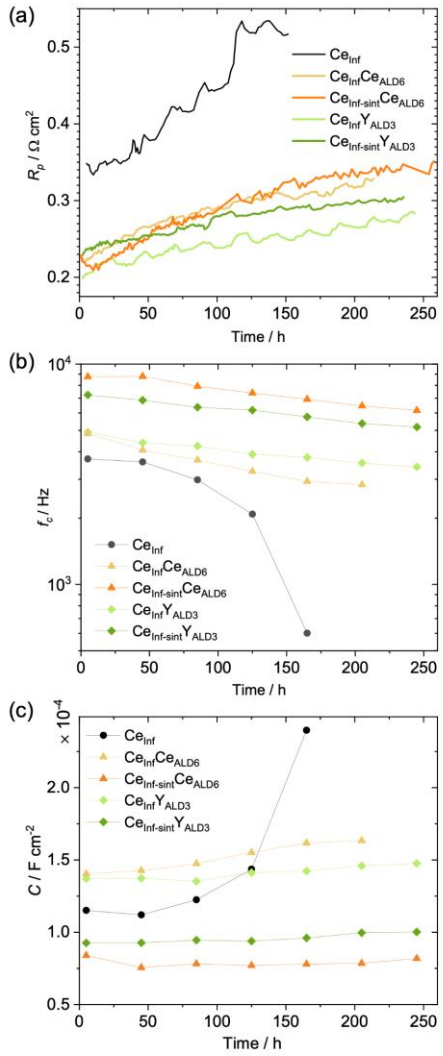

Fig. 5 (a) Time evolution of polarization resistance (R_p), (b) characteristic frequency (f_c), and (c) capacitance (C). All are deduced from the impedance data, which were obtained intermittently at the open circuit condition during the thermal exposure at 700 °C.

The ALD treatment on an infiltrated electrode is also found to improve the thermal stability of the electrode significantly. As shown in Fig. 5a, $\mathrm{Ce_{Inf}}$ shows a rapid degradation; R_p changed

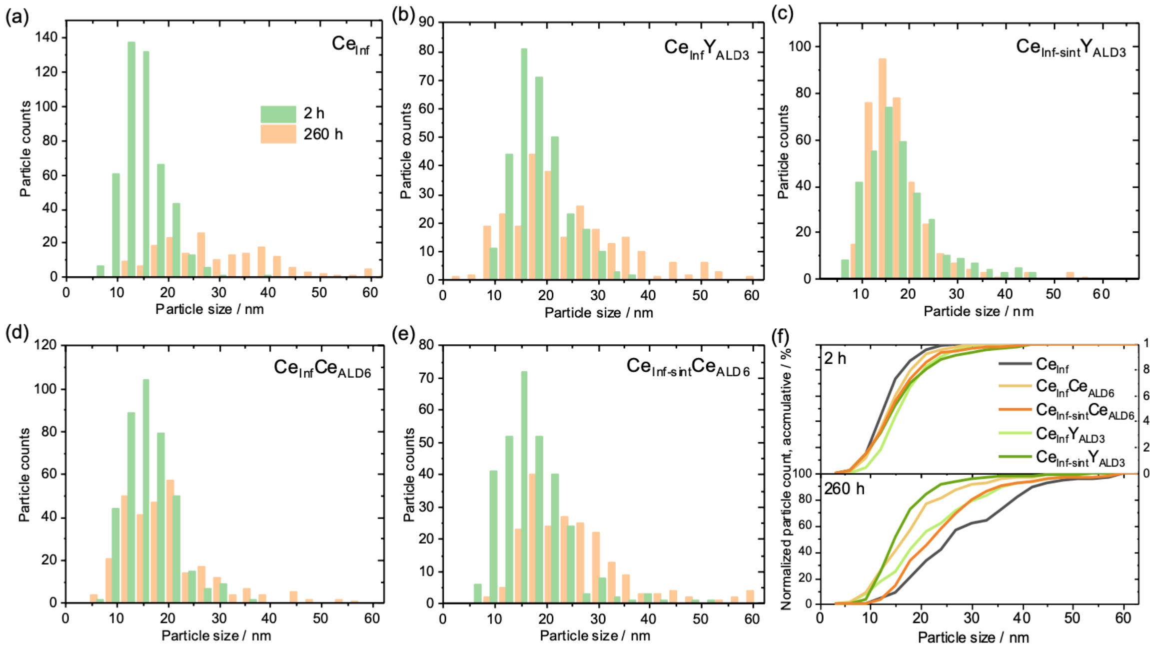

Fig. 6 (a-e) Size distribution of infiltrated ceria NPs in each sample after 2 h and 260 h at 700 °C, and (f) the corresponding accumulative distribution of infiltrated ceria NPs, counting from smaller NPs. Graphs are based upon the SEM images provided in Figs. S12 and S13; see SI "Quantification of infiltrated particle sizes" section for details.

from 0.33 to 0.53 Ω cm^2 in 150 h at 700 °C, which translates into a degradation rate of 1.33 mΩ cm^2 h^{-1}. By treating the infiltrated surface with ALD (Type III), however, we observe a significantly improved thermal stability. By coating 6 ALD cycles of ceria (Ce$_{Inf}$Ce$_{ALD6}$), the degradation rate decreased to 0.48 mΩ cm^2 h^{-1} (from 0.22 to 0.32 Ω cm^2 in 200 h), and 3 cycles of yttria (Ce$_{Inf}$Y$_{ALD3}$) resulted in an even lower degradation rate of 0.30 mΩ cm^2 h^{-1} (from 0.21 to 0.27 Ω cm^2 in 220 h). The enhanced durability is further visualized with the evolution of characteristic frequencies (f_c) and capacitance (C) of electrode process as shown in Figs. 5b and 5c; here, the capacitance is quantified using $C = (R_p \cdot Q)^{1/\alpha}/R_p$ where Q is a non-ideal capacitance specific to CPEs and α is the similarity to an ideal capacitor (α = 1: an ideal capacitor). While Ce$_{Inf}$ exhibits a dramatic shift in f_c in 150 h (from 3,713 Hz to 601 Hz), ALD-treated samples show relatively mild changes (Ce$_{Inf}$Ce$_{ALD6}$: from 4,841 to 2,835 Hz in 200 h; Ce$_{Inf}$Y$_{ALD3}$: from 4,916 to 3,417 Hz in 250 h), confirming the enhanced thermal stability by ALD treatment. All the Type III samples maintain the f_c values within $10^3 - 10^4$ Hz and the capacitance values within $0.7 \times 10^{-4} - 1.6 \times 10^{-4}$ F cm^{-2} throughout the thermal exposure. Combined with the initial m values of ~0.15 (Fig. 4e), it can be reasonably asserted that the RDS of all the studied Type III samples is O_2 dissociation combined with an electron transfer process (i.e. O_2 activation); see SI "Effect of surface treatment on the RDS" section for details. However, the non-ALD treated Ce$_{Inf}$ shifts its f_c to a much lower values over time suggesting the RDS shifts to a more sluggish, non-electrochemical process such as surface diffusion of electroactive oxygen.[21]

The degradation of infiltrated SOFC cathodes has been ascribed largely to the agglomeration of infiltrated NPs, hence the loss of active surface area.[25] In light of this, we examined the change in the size of infiltrated NPs by an extended thermal exposure at 700 °C for 260 h. The test was performed in a Cr-free chamber, eliminating Cr poisoning[32] from a possible factor of cell degradation. Figs. 6a-e show the size distribution of infiltrated NPs at the initial (2 h) and final stage (260 h) of the thermal stress. The bar charts show that even 3 – 6 cycles of ALD treatment (corresponding to the nominal thickness of 0.72 – 1.44 Å) is highly effective in suppressing agglomeration. While the distribution of Ce$_{Inf}$ shifted prominently toward larger sizes after 260 h (Fig. 6a), those of ALD-treated samples (Figs. 6b-e) are much better preserved during the same duration. For a quantitative analysis, accumulative distributions of NP sizes in each sample are given in Fig. 6f. It is quantified that 80% of the infiltrated ceria NPs in Ce$_{Inf-sint}$Y$_{ALD3}$ are equal to or less than 20.9 nm (namely, d_{80} = 20.9 nm) at the initial stage (2 h), and the d_{80} value quantified at the final stage (260 h) is virtually unaltered (22.2 nm), indicating that Ce$_{Inf-sint}$Y$_{ALD3}$ exhibits an excellent resistance against thermal agglomeration of infiltrated NPs. In terms of agglomeration resistance among the Type III samples as gauged by the average d_{80} value change per hour (Δd_{80}/h) in [pm h^{-1}], Ce$_{Inf-sint}$Y$_{ALD3}$ (5.0) is followed by Ce$_{Inf}$Ce$_{ALD6}$ (24.2), Ce$_{Inf}$Y$_{ALD3}$ (36.5) and Ce$_{Inf-sint}$Ce$_{ALD6}$ (39.2). On the other hand, d_{80} of Ce$_{Inf}$ changed significantly from 16.7 nm to 38.4 nm in ~ 260 h (Δd_{80}/h = 83.5 pm h^{-1}), reflecting the most severe NP growth among the 5 samples. (The d_{80} values are tabulated in Table S5.) These proves that an ALD overcoat is an effective inhibitor of sintering process. A sintering process can be depicted as the migration of atoms along the surface of a material driven by chemical potential gradient, eventually in the direction of minimizing the overall surface energy of the structure.[33] The ALD overcoat, albeit angstrom-scale, should have uniformly covered the infiltrated NPs and effectively deterred the detachment, diffusion and attachment of atomic species in the infiltrated NPs. As aforementioned, unlike the other samples, Ce$_{\text{Inf-sint}}$Ce$_{\text{ALD6}}$ exhibits a number of nanodots accumulated particularly at the interfaces between infiltrated NPs (i.e. at the "necks") after a long-term thermal exposure at 700 °C for 260 h (as shown in Fig. S13e and Fig. S1a-b). The initially uniform ceria overcoat by ALD in Ce$_{\text{Inf-sint}}$Ce$_{\text{ALD6}}$ (as shown in Fig. S12e where no nanodot-like feature is found) is believed to have evolved into nanodot clusters, which migrated preferentially to the necks to minimize its surface energy during the heating.[34] We conjecture that the nanodot clusters themselves are susceptible to further sintering if an extended thermal input were provided, and thus eventually incapable of protecting their underlying NPs against sintering. For this reason, the ALD overcoat that does not develop the nanodot cluster-like features during extended operation is likely to be advantageous in a prolonged protection of its underlying NPs. This is where an extended durability test can be highly valuable in further clarifying the effectiveness of ALD treatment in maintaining long-term functionality.

Finally, as seen from Fig. 5 and Fig. 6, there is a clear positive correlation between the durability of electrochemical performance and thermal stability of electrode morphology; the samples with the highest and the lowest agglomeration rate (Ce$_{\text{Inf-sint}}$Y$_{\text{ALD3}}$ and Ce$_{\text{Inf}}$, respectively; from Fig. 6) are concomitantly those with the highest and the lowest rate of performance degradation (from Fig. 5). From these, we conclude that an angstrom-level ALD treatment is highly effective in suppressing the agglomeration kinetics of underlying infiltrated NPs, which directly affects long-term durability of electrode performance. While the main focus was made on the NP agglomeration as the factor of electrode degradation (by choosing Sr-free electrode materials and performing the thermal stability test in a Cr-free chamber), the beneficial effect of ALD treatment can be also leveraged to address other major SOFC degradation mechanisms such as Sr segregation[35] and Cr poisoning.[32] While Cr poisoning is intrinsically a surface process (i.e. a process that occurs on the surface of an electrode), Sr segregation is driven by bulk phenomena such as electrostatic interaction and lattice strain.[14] However, recent reports suggests that Sr segregation can be effectively tuned by a surface-specific treatment.[14,15,36] In this regard, we believe this study lays a solid foundation for additional insights related to the impact of highly surface-specific engineering on the performance and durability of solid oxide-based high temperature systems.

Conclusions

While infiltrated NPs on a porous backbone often enhances the electrode performance by a significant margin, the high surface energy of NPs tends to make them highly susceptible to thermal agglomeration. In this report, we show that an ALD-based atomic-scale (0.7 – 1.5 Å) overcoat of ceria or yttria over a ceria infiltrated LNF is highly effective in suppressing the thermal agglomeration of infiltrated ceria NPs, and that the effect is directly correlated to the thermal durability of electrode performance, via a systematic and quantitative approach. In addition, we demonstrate that the atomic-scale ALD overcoat dramatically enhances the electrode performance in terms of polarization resistance and its activation energy for both bare LNF and ceria-infiltrated LNF electrodes. The improved electrode activity from ALD treatment is mainly ascribed to a significant facilitation of O_2 activation (i.e. O_2 dissociation followed by a partial reduction) by the additional surface-specific oxygen-deficient and catalytically active ceria.

Conflicts of interest

There are no conflicts to declare.

Acknowledgements

The authors acknowledge the support from the Korea Institute of Industrial Technology (KITECH) and U.S. National Science Foundation CAREER Award (DMR 1753383). The use of TEM at the Molecular Foundry was supported by the U.S. Department of Energy (Contract No. DE-AC02-05CH11231). The XPS work was performed under the auspices of the U.S. Department of Energy by Lawrence Livermore National Laboratory (Contract DE-AC52-07NA27344).

Notes and references

1 R. M. Ormerod, *Chem. Soc. Rev.*, 2003, **32**, 17–28.
2 D. J. L. Brett, A. Atkinson, N. P. Brandon and S. J. Skinner, *Chem. Soc. Rev.*, 2008, **37**, 1568.
3 Z. Shao, W. Zhou and Z. Zhu, *Prog. Mater. Sci.*, 2012, **57**, 804–874.
4 R. Pelosato, G. Cordaro, D. Stucchi, C. Cristiani and G. Dotelli, *J. Power Sources*, 2015, **298**, 46–67.
5 Z. Jiang, C. Xia and F. Chen, *Electrochim. Acta*, 2010, **55**, 3595–3605.
6 S. P. Jiang, *Int. J. Hydrogen Energy*, 2012, **37**, 449–470.
7 A. Karimaghaloo, J. Koo, H.-S. Kang, S. A. Song, J. H. Shim and M. H. Lee, *Int. J. Precis. Eng. Manuf. Technol.*, 2019, **6**, 611–628.
8 B. J. O'Neill, D. H. K. Jackson, J. Lee, C. Canlas, P. C. Stair, C. L. Marshall, J. W. Elam, T. F. Kuech, J. A. Dumesic and G. W. Huber, *ACS Catal.*, 2015, **5**, 1804–1825.
9 S. M. George, *Chem. Rev.*, 2010, **110**, 111–131.
10 I. Chang, S. Ji, J. Park, M. H. M. H. Lee and S. W. S. W. Cha, *Adv. Energy Mater.*, 2015, **5**, 1402251.
11 A. Karimaghaloo, A. M. A. M. Andrade, S. Grewal, J. H. J. H. Shim and M. H. M. H. Lee, *ACS Omega*, 2017, **2**, 806–813.
12 J. W. Shin, S. Oh, S. Lee, J.-G. Yu, J. Park, D. Go, B. C. Yang, H. J. Kim and J. An, *ACS Appl. Mater. Interfaces*, 2019, **11**, 46651–46657.
13 Y. Chen, L. Liang, S. A. Paredes Navia, A. Hinerman, K.

Gerdes and X. Song, *ACS Catal.*, 2019, **9**, 6664–6671.

14 Y. Wen, T. Yang, D. Lee, H. N. Lee, E. J. Crumlin and K. Huang, *J. Mater. Chem. A*, 2018, **6**, 24378–24388.

15 Y. Gong, D. Palacio, X. Song, R. L. Patel, X. Liang, X. Zhao, J. B. Goodenough and K. Huang, *Nano Lett.*, 2013, **13**, 4340–5.

16 H. J. Choi, K. Bae, S. Grieshammer, G. D. Han, S. W. Park, J. W. Kim, D. Y. Jang, J. Koo, J.-W. Son, M. Martin and J. H. Shim, *Adv. Energy Mater.*, 2018, **8**, 1802506.

17 Y. Li, W. Zhang, Y. Zheng, J. Chen, B. Yu, Y. Chen and M. Liu, *Chem. Soc. Rev.*, 2017, **46**, 6345–6378.

18 T. Ohzeki, T. Hashimoto, K. Shozugawa and M. Matsuo, *Solid State Ionics*, 2010, **181**, 1771–1782.

19 T. Komatsu, H. Arai, R. Chiba, K. Nozawa, M. Arakawa and K. Sato, *J. Electrochem. Soc.*, 2007, **154**, B379.

20 N. Q. Minh, *J. Am. Ceram. Soc.*, 1993, **76**, 563–588.

21 H.-S. Kang, S. Grewal, H. Li and M. H. Lee, *J. Electrochem. Soc.*, 2019, **166**, F255–F263.

22 T. A. Schmauss, J. G. Railsback, M. Y. Lu, K. Y. Zhao and S. A. Barnett, *J. Mater. Chem. A*, 2019, **7**, 27585–27593.

23 A. Gupta, T. S. Sakthivel, C. J. Neal, S. Koul, S. Singh, A. Kushima and S. Seal, *Biomater. Sci.*, 2019, **7**, 3051–3061.

24 K. I. Maslakov, Y. A. Teterin, A. J. Popel, A. Y. Teterin, K. E. Ivanov, S. N. Kalmykov, V. G. Petrov, P. K. Petrov and I. Farnan, *Appl. Surf. Sci.*, 2018, **448**, 154–162.

25 P. A. Connor, X. Yue, C. D. Savaniu, R. Price, G. Triantafyllou, M. Cassidy, G. Kerherve, D. J. Payne, R. C. Maher, L. F. Cohen, R. I. Tomov, B. A. Glowacki, R. V. Kumar and J. T. S. Irvine, *Adv. Energy Mater.*, 2018, **8**, 1800120.

26 J. Y. Chen, J. Rebello, V. Vashook, D. M. Trots, S. R. Wang, T. L. Wen, J. Zosel and U. Guth, *Solid State Ionics*, 2011, **192**, 424–430.

27 M. Bevilacqua, T. Montini, C. Tavagnacco, E. Fonda, P. Fornasiero and M. Graziani, *Chem. Mater.*, 2007, **19**, 5926–5936.

28 S. P. Jiang and W. Wang, *J. Electrochem. Soc.*, 2005, **152**, A1398.

29 Z.-K. Han, L. Zhang, M. Liu, M. V. Ganduglia-Pirovano and Y. Gao, *Front. Chem.*, 2019, **7**, 436.

30 S. Zhao, L. Yan, H. Luo, W. Mustain and H. Xu, *Nano Energy*, 2018, **47**, 172–198.

31 J. Paier, C. Penschke and J. Sauer, *Chem. Rev.*, 2013, **113**, 3949–3985.

32 S. P. Jiang and X. Chen, *Int. J. Hydrogen Energy*, 2014, **39**, 505–531.

33 E. D. Goodman, J. A. Schwalbe and M. Cargnello, *ACS Catal.*, 2017, **7**, 7156–7173.

34 R. K. Bordia, S.-J. L. Kang and E. A. Olevsky, *J. Am. Ceram. Soc.*, 2017, **100**, 2314–2352.

35 W. Lee, J. W. Han, Y. Chen, Z. Cai and B. Yildiz, *J. Am. Chem. Soc.*, 2013, **135**, 7909–7925.

36 N. Tsvetkov, Q. Lu, L. Sun, E. J. Crumlin and B. Yildiz, *Nat. Mater.*, 2016, **15**, 1010–1016.